

Cite this: *RSC Adv.*, 2015, 5, 33981

# Robust reduced graphene oxide paper fabricated with a household non-stick frying pan: a large-area freestanding flexible substrate for supercapacitors†

Yang Huang,<sup>a</sup> Minshen Zhu,<sup>a</sup> Wenjun Meng,<sup>a</sup> Yuqiao Fu,<sup>a</sup> Zifeng Wang,<sup>a</sup> Yan Huang,<sup>a</sup> Zengxia Pei<sup>a</sup> and Chunyi Zhi<sup>\*ab</sup>

Inspired by cooking omelettes, a facile, low-cost and scalable method involving the use of a readily available household non-stick frying pan is introduced to fabricate large-area freestanding reduced graphene oxide (RGO) paper. The as-fabricated RGO paper is robust enough to bear sandpaper polishing, bending/folding, and hydrothermal and electrochemical deposition processes without obvious structure/performance degradation. As a demonstration, the as-obtained RGO papers were directly used as universal flexible substrates for high performance supercapacitors (SCs). Thus, WO<sub>3</sub> and PPy, which are two distinctive active materials, were loaded onto the RGO paper *via* a hydrothermal process and electrodeposition process, respectively, which are two typical fabrication methods for high performance SC electrodes. The resultant WO<sub>3</sub>- and PPy-RGO paper, which act as negative and positive electrodes, respectively, were further assembled into a flexible asymmetric supercapacitor (ASC), achieving a high energy density of 0.23 mW h cm<sup>-3</sup> at a power density of 7.3 mW cm<sup>-3</sup> when normalized to the whole volume. Moreover, benefiting from the robust flexible RGO substrate, the performance of the ASC showed great stability under different bending angles and after repeated bending/folding. These exciting results demonstrate that our robust RGO paper is an ideal universal substrate for different active materials synthesized *via* various processing methods, which show its great potential in an all-solid energy storage system with excellent flexibility and robustness.

Received 14th February 2015

Accepted 27th March 2015

DOI: 10.1039/c5ra02868j

www.rsc.org/advances

## 1. Introduction

The rapid rise of personal electronics, especially the ever-increasing demand for wearable electronics, has prompted the development of lightweight, flexible, and highly efficient energy storage devices.<sup>1,2</sup> In accordance with this trend, a variety of flexible all-solid supercapacitors (SCs) combined with exceptionally long cycle life, enhanced high power and energy density, good operational safety and environmental benign nature have been designed and are currently being fabricated.<sup>3,4</sup> For high performance flexible SCs, special attention has been dedicated to the design of flexible electrodes, and two main kinds of strategies have been developed, namely, (i) fabricating flexible hybrid electrodes of active materials<sup>5,6</sup> and (ii) fabricating freestanding conductive substrates to support active materials.<sup>7,8</sup> Compared with hybrid electrodes, the use of substrates is more attractive, not only because of their low cost

and high flexibility, but also, more importantly, because they are more universal and their use could open up the possibility to support any upcoming active material with enhanced performance *via* different processing methods.

Recently, metals,<sup>4</sup> carbon-based materials,<sup>9</sup> textiles,<sup>10</sup> sponges<sup>11</sup> and even conventional paper<sup>12,13</sup> have been used as substrates to fabricate high performance flexible SCs. Among these, graphene-based materials, one of the most commonly reported carbon materials lately, have attracted significant attention owing to their outstanding electronic, mechanical, and thermal properties,<sup>14,15</sup> which can lead to a wide range of applications such as conducting transparent electrodes,<sup>16</sup> electrochemical batteries,<sup>17</sup> sensors,<sup>18</sup> and SCs.<sup>19</sup> Because of their 2-dimensional properties, these graphene-based materials can be easily assembled into macroscopic paper-like structures, making them an ideal flexible substrate for loading active materials. Generally, there are two main approaches for obtaining graphene-based paper: one is by direct production using reduced graphene oxide (RGO),<sup>6,20</sup> and the other is to rely on the post-reduction of pre-fabricated GO paper.<sup>21</sup> However, current strategies for the production of freestanding RGO paper substrates are far from satisfactory, since they are usually time consuming (*e.g.* membrane filtration)<sup>6</sup> and/or require custom accessories or delicate equipment (*e.g.* electrophoretic

<sup>a</sup>Department of Physics and Materials Science, City University of Hong Kong, 83 Tat Chee Avenue, Kowloon, Hong Kong, P. R. China. E-mail: cy.zhi@cityu.edu.hk; Fax: +852-3442-0538; Tel: +852-3442-7891

<sup>b</sup>Shenzhen Research Institute, City University of Hong Kong, Shenzhen, P. R. China

† Electronic supplementary information (ESI) available. See DOI: 10.1039/c5ra02868j

deposition and chemical vapor deposition (CVD)),<sup>22,23</sup> which may impede their further development in large-scale fabrication applications. Obviously, the most important obstacle is to achieve a large-area RGO paper *via* a simple method with high efficiency.

Herein, we develop an ingenious method to fabricate a large-area freestanding RGO paper by using common household utensils, which is demonstrated to be a facile, low cost and scalable method that was inspired by cooking an omelette. After successful post-reduction, the obtained RGO paper exhibits excellent mechanical and electrical properties, as well as good compatibilities with many different active materials and processing methods, which enable it to be directly used as a robust substrate for high performance SCs. As a demonstration, two distinctive active materials ( $\text{WO}_3$  and PPy) were loaded on to an RGO substrate perfectly *via* hydrothermal and electrodeposition methods, which are the two typical synthesis methods for SC electrodes. These two resultant flexible electrodes were further assembled into high performance all-solid asymmetric supercapacitors (ASCs) and were able to achieve a high energy density of  $0.23 \text{ mW h cm}^{-3}$  at a power density of  $7.3 \text{ mW cm}^{-3}$ . Moreover, these ASCs showed no degradation under different bending angles and remained stable even after hundreds of times of being bent, together with excellent cycling stability (retaining 99.4% after 2000 cycles). Therefore, the RGO paper, with excellent flexibility and robustness, is proven to be an ideal universal substrate for various active materials synthesized *via* different processing methods, thus showing great potential for various portable/wearable electronics.

## 2. Experimental section

### 2.1 Fabrication of the RGO paper

GO was prepared from purified natural graphite by using a modified Hummers method.<sup>24</sup> A suspension of GO sheets was obtained by ultrasonic exfoliation of the as-prepared GO in deionized (DI) water, followed by centrifugation at 5000 rpm for 10 min to remove the non-exfoliated sheets.

Our ingenious fabrication of a large area freestanding RGO paper was inspired by the daily cooking of an omelette, as shown in the schematic in Fig. 1A. First, an adequate amount of GO suspension ( $5 \text{ mg mL}^{-1}$ , 100 mL), a viscous liquid similar to egg liquid, was poured directly into a common household non-stick frying pan (IKEA, with a diameter of 20 cm) using a spatula to ensure even spreading. Then, the frying pan was placed on an induction cooker and kept under appropriate heating conditions (60 W, 80–90 °C) until the GO suspension was dried, normally requiring 2–3 hours. It is suggested that the heating temperature is maintained under 100 °C, since small pores will form if the suspension solution boils. Then, the GO paper was easily peeled off from the frying pan and reduced into RGO paper by immersing into a hydrohalic acid (HI) solution in a sealed cuvette.<sup>21</sup> Finally, the large area freestanding RGO paper was annealed at 750 °C under an argon flow of  $50 \text{ mL min}^{-1}$  for 2 h, which was employed for elimination of the introduced sub-products ( $\text{I}^-$  ions), while also providing extra reduction.

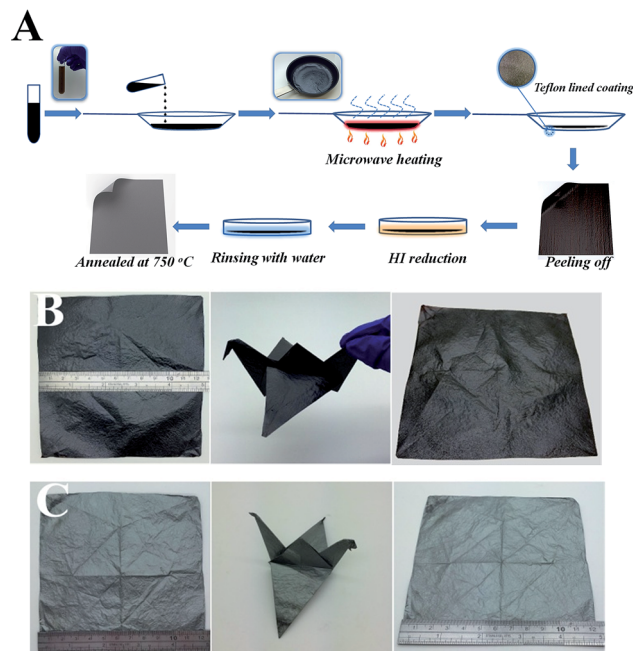


Fig. 1 (A) Schematic representation of a proposed fabrication process of large-area freestanding RGO paper *via* the use of common household utensils. An homogeneous GO suspension solution is directly poured into a non-stick frying pan, and dried with moderate heating. After the suspension is dried, the GO paper is easily peeled off and reduced into RGO paper with HI solution and by thermal annealing. (B) Photographs of a large-area freestanding dark brown GO paper (left), folded into an origami crane (centre) and the extension GO paper after origami crane folding (right) (about  $12 \text{ cm} \times 12 \text{ cm}$ ,  $144 \text{ cm}^2$ ). (C) Photographs of a large-area freestanding silver RGO paper (left), folded into an origami crane (centre), and the extension RGO paper after the origami crane folding (right) (about  $12 \text{ cm} \times 12 \text{ cm}$ ,  $144 \text{ cm}^2$ ).

### 2.2 Fabrication of $\text{WO}_3$ - and PPy-RGO paper

The RGO paper was first cut into an appropriate size (e.g.  $5 \text{ cm} \times 2 \text{ cm}$ ) and polished with sandpaper (P1000) in order to obtain a unique fish scale-like structure. The pre-treated paper was washed with DI water and dried prior to use.

The  $\text{WO}_3$ -RGO paper electrode was prepared by a hydrothermal method, using RGO paper as the substrate according to a previous report.<sup>25</sup> 10 mL of 0.3 M HCl was slowly added into the 10 mL solution containing 0.6 g  $\text{Na}_2\text{WO}_4 \cdot 2\text{H}_2\text{O}$ , and then 0.6 g NaCl was added into the solution. Subsequently, the RGO paper was immersed in the resultant solution and transferred into a Teflon-lined stainless autoclave, and then heated at 180 °C for 12 h. After the autoclave cooled down to room temperature, the RGO paper was taken out, rinsed with DI water and dried prior to use. The precipitates were collected by centrifugation (5000 rpm), washed with DI water and absolute ethanol several times, and then finally dried overnight.

The PPy-RGO paper electrode was prepared by an electrodeposition method using a three-electrode configuration with RGO paper as the working electrode, platinum mesh as the counter electrode, and Ag/AgCl as the reference electrode. In brief, the electrodeposition solution contained 300  $\mu\text{L}$  distilled pyrrole monomer, 0.1 M *p*-toluenesulfonic acid, 0.3 M sodium

dodecylbenzenesulfonate and 60 mL DI water. A constant voltage of 0.8 V was used during the deposition process and lasted for 90 s. Then the PPy-RGO paper was washed with DI water and dried prior to use.

### 2.3 Assembly of WO<sub>3</sub>-RGO//PPy-RGO ASC

The WO<sub>3</sub>- and PPy-RGO papers, acting as the negative and positive electrodes, were assembled into an ASC by using PVA-H<sub>2</sub>SO<sub>4</sub> as the solid electrolyte. The PVA-H<sub>2</sub>SO<sub>4</sub> gel electrolyte was first prepared by dissolving PVA powder (6 g) in DI water (60 mL) and H<sub>2</sub>SO<sub>4</sub> (6 g). The mixture was heated to 150 °C with vigorous stirring until a transparent solution formed. Then, the RGO-based electrodes were coated with a thin layer of PVA-H<sub>2</sub>SO<sub>4</sub> gel electrolyte and dried under vacuum at room temperature. Afterwards, another thin layer of gel electrolyte was coated on one of the resultant electrodes, by pasting the other onto it gently and then drying in air. Thus, a flexible all-solid ASC was obtained.

### 2.4 Materials characterization and electrochemical measurements

The morphology of the samples was investigated with an environmental scanning electron microscope (ESEM, FEI/Philips XL30). X-ray diffraction (XRD) patterns were collected with a BRUKER D2 PHASER diffractometer equipped with CuK<sub>α</sub> irradiation ( $\lambda = 1.54184 \text{ \AA}$ , 30 kV and 10 mA). X-ray photoelectron spectroscopy (XPS) measurements were performed on an ESCALAB 220i-XL electron spectrometer with monochromatic Al K<sub>α</sub> X-ray radiation and a hemispherical electron energy analyzer. Raman spectra were excited with a laser of 523 nm and recorded with a Labram spectrometer. The electrical conductivity of the RGO paper was measured by a standard four-probe method. Mechanical property measurements were performed on strips of the papers with an Instron 5661 tester (tensile rate = 0.020 mm min<sup>-1</sup>). Sample widths were measured by a vernier caliper, while the thicknesses were measured on the fracture edges with SEM. Electrochemical measurements, including cyclic voltammetry (CV) curves, galvanostatic charge-discharge curves, and electrochemical impedance spectroscopy (EIS, 100 kHz–0.05 Hz) were conducted on a CHI 760e electrochemical workstation (CH Instruments Company). The electrochemical performances of the individual electrodes were investigated using a conventional three electrode system (with Pt mesh as the counter electrode and Ag/AgCl as the reference electrode) in 1 M H<sub>2</sub>SO<sub>4</sub> prior to assembling of the ASC. The performance of the ASC was measured using a two-electrode method.

### 2.5 Calculations

The areal ( $C_s$ , F cm<sup>-2</sup>) and specific ( $C_m$ , F g<sup>-1</sup>) capacitance of the positive and negative electrodes in the three electrode configuration were calculated from the corresponding charge-discharge curves at different current densities according to eqn (1):

$$C_s = I\Delta t/s\Delta V \text{ or } C_m = I\Delta t/m\Delta V \quad (1)$$

where  $I$  (A) is the discharge current,  $\Delta t$  (s) is the discharge time,  $s$  is the specific area (cm<sup>2</sup>),  $m$  (g) is the total mass of the electrode, and  $\Delta V$  (V) is the discharge voltage range (excluding the  $iR$  drop).

The capacitance values of the ASC were calculated from the corresponding CV curves at different scan rates according to eqn (2):

$$C_{\text{device}} = \frac{1}{\nu(V_f - V_i)} \int_{V_i}^{V_f} I(V) dV \quad (2)$$

where  $C_{\text{device}}$  is denoted as the capacitance contribution from the asymmetric electrodes,  $\nu$  is the scan rate (V s<sup>-1</sup>),  $V_f$  and  $V_i$  are the integration potential limits of the voltammetric curve and  $I(V)$  is the voltammetric discharge current. The specific capacitances were calculated based on the areal or the whole volume of the device according to the following equation:

$$C_s = C_{\text{device}}/A \text{ or } C_v = C_{\text{device}}/V \quad (3)$$

where  $C_s$  (F cm<sup>-2</sup>) and  $C_v$  (F cm<sup>-3</sup>) refer to the areal capacitance and the volumetric stack capacitance of the ASC, respectively, and  $A$  and  $V$  are the total area (cm<sup>2</sup>) and volume (cm<sup>3</sup>) of the device. The areal capacitance was calculated based on the entire projected surface area of the device. The volumetric stack capacitance was calculated by taking into account the whole device, including the solid electrolyte. A charge balance between negative and positive electrodes is obtained by the equation:  $C_-V_- = C_+V_+$ , where  $C_-$  and  $C_+$  are the capacitance of the negative and positive electrodes, respectively, and  $V_-$  and  $V_+$  are the potential window of the negative and positive electrodes, respectively.

The volumetric energy density of the ASC was obtained from the following equation:

$$E_v = \frac{1}{2} \times C_v \times \frac{(\Delta V)^2}{3600} \quad (4)$$

where  $E_v$  (W h cm<sup>-3</sup>) is the volumetric energy density,  $C_v$  is the volumetric stack capacitance obtained from eqn (3) and  $\Delta V$  (V) is the discharge voltage range.

The power density of the device was calculated from the following equation:

$$P_v = \frac{E_v}{\Delta t} \times 3600 \quad (5)$$

where  $P_v$  (W cm<sup>-3</sup>) is the volumetric power density,  $E_v$  is the volumetric energy density obtained from eqn (4) and  $\Delta t$  (s) is the discharge time.

## 3. Results and discussion

### 3.1 Fabrication of large area freestanding RGO paper

As shown in Fig. 1A, when the water keeps evaporating under continuous heating and leads to a higher and higher GO concentration, the supersaturated GO sheets floating on the surface will aggregate together and self-stack into a thin film because of the increasing sheet-to-sheet interaction, thus ultimately forming a layer-by-layer GO paper. Because of the Teflon-

lined coating, the dried dark brown round-shaped GO paper can be easily peeled off from the frying pan (Fig. S1†). Then, this GO paper can be easily reduced into a highly conductive RGO paper with HI solution and by thermal annealing. Based on this ingenious method, large-area freestanding flexible RGO papers with a variety of sizes and thicknesses can be obtained by just changing to non-stick pans of different sizes or by simply adjusting the volume and concentration of the GO suspension. As a demonstration, a GO paper with a surface area of 144 cm<sup>2</sup> was made and could be folded into an origami crane. After unfolding, amazingly, there were only several creases left on the paper. (Fig. 1B) Then, this pristine GO paper was reduced into RGO paper by the aforementioned methods. The RGO paper demonstrated similar flexibility and toughness with the pristine GO paper, showing no defects even after complex folding (Fig. 1C). When compared to other reported fabrication methods for RGO paper,<sup>22,26–30</sup> our ingenious approach has many advantages: (i) it is convenient and easy to scale up as the equipment is a common household non-stick frying pan, which is readily available; (ii) there is a possibility to fabricate RGO papers with multiple sizes; (iii) it is efficient and evaporation of water from the GO suspension exhibits a satisfactory efficiency, especially compared with the traditional time-consuming, vacuum-assisted flow-filtration methods; and (iv) it is cost-effective since the frying pan can be readily reused after cleaning, and thus the cost is extremely low.

### 3.2 Characterization

The deoxygenation and interlaminar consolidation of the as-prepared papers was proven by the detailed characterization of XRD and XPS. As shown in Fig. 2A, the XRD pattern of the GO paper presents a diffraction peak at  $2\theta = 9.38^\circ$ , suggesting a larger interlayer spacing (0.94 nm) due to the presence of oxygen-containing functional groups (*e.g.* epoxy and hydroxyl groups) attached to the GO sheet surface and molecules of water coming from the harsh oxidation applied.<sup>31</sup> In the case of RGO paper, the diffraction peak of RGO is shifted to  $25.64^\circ$ , becoming narrower and sharper, not only indicating a significant reduction of the interlayer distance (0.35 nm) owing to the elimination of oxygen-containing groups, but also revealing the more regular packing of graphene layers with a longer correlation length due to the coalescence of the graphene sheets.<sup>21</sup> The high resolution of the C1s peaks in the XPS of the RGO paper also proves that the oxygen-containing groups have been removed (Fig. 2B). Deconvolution of the C1s spectrum in the pristine GO paper reveals that it consists of two main components arising from C–O (hydroxyl and epoxy,  $\sim 286.3$  eV) and C–O–C ( $\sim 286.9$  eV) and one minor component C=O/O–C=O (carbonyl,  $\sim 288.3$  eV). After the post-reductions, it is clear that the majority of the oxygen-containing groups in the pristine GO paper are almost all removed and the C–C/C=C bonds then become dominant ( $\sim 284.7$  eV) in the RGO paper, as shown by the one single peak with a small tail in the higher binding energy region in Fig. 2B. The surface C/O atomic ratio detected by XPS is  $\sim 2.8$  for the pristine GO paper and is increased to

$\sim 12.5$  after the post-reductions, strongly indicating the complete elimination of the oxygen groups.

The removal of the oxygen-containing groups leads to greater connectivity among the existing graphitic domains by the formation of new sp<sup>2</sup> clusters,<sup>32</sup> which can also be followed by Raman spectroscopy. The G-band (at 1585 cm<sup>−1</sup>) is known to be a characteristic of the sp<sup>2</sup>-hybridized carbon–carbon bonds in graphene.<sup>33,34</sup> Moreover, the presence of the D-band (at 1350 cm<sup>−1</sup>) indicates structural imperfections induced by the attachment of oxygen-containing functional groups on the carbon basal plane.<sup>34</sup> As a result, the  $I_D/I_G$  ratio is widely used to provide structural information on the GO with different degrees of reduction, while a high  $I_D/I_G$  is related to the presence of disordered carbon and/or functionalities attached to graphene sheets. Compared with GO paper, the intensity of the D-band peak in RGO paper is clearly reduced and the  $I_D/I_G$  ratio is decreased notably from 1.31 to 0.82, suggesting the extensive repairing of defects created by the attachment of oxygen groups.

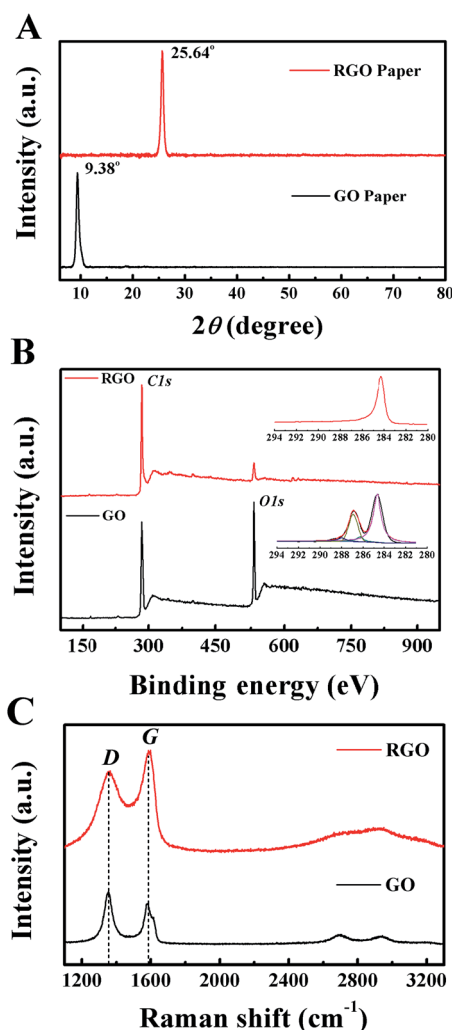


Fig. 2 (A) XRD patterns of the GO and RGO papers. (B) High-resolution XPS spectra (C1s) of the GO and RGO papers. (The position of C–C/C=C, C–O, C–O–C, and C=O/O–C=O is 284.7 eV, 286.3 eV, 286.9 eV and 288.3 eV). (C) Raman spectra of the GO and RGO papers collected with a laser of 532 nm.



Owing to restoration of the  $sp^2$  carbon network in the GO sheets and the decrease in the interlayer distance, as revealed in the structural characterization, the interaction among the reduced GO sheets in RGO paper is increased; thus, the electrical conductivity and mechanical strength of the RGO paper are greatly improved. The conductivities of the RGO paper were measured by a collinear four-point probe method, and a high value for electrical conductivity was achieved by our progressive reduction, reaching as high as  $203.7 \text{ S cm}^{-1}$ . Due to the increased neighbouring coalescence interactions between the RGO sheets, the RGO paper has a modulus of 1.65 GPa and a strength of 9.41 MPa, which is 11 times and 21 times more than that of the pristine GO paper (modulus 0.13 GPa, strength 0.41 MPa) (Fig. 3A). Accordingly, RGO paper presents outstanding flexibility and toughness, as shown in Fig. 1C. To further investigate whether the good electrical conductivity of the RGO paper is in agreement with its robust body, cycled bending tests of the resistance were operated by a designed stepper motor. It is very impressive that the resistance showed no observable change after repeated bending for over 1000 times (Fig. 3B), indicating that the good electrical conductivity was integrated with its robust body. Good electrical conductivity, together with excellent mechanical strength, is important for applying the flexible substrates to high-performance SC electrodes, as they can ensure that the substrate can bear various post-treatments and fabrication processes.<sup>35</sup> Based on the above demonstrations, our RGO paper should be an ideal substrate for SCs.

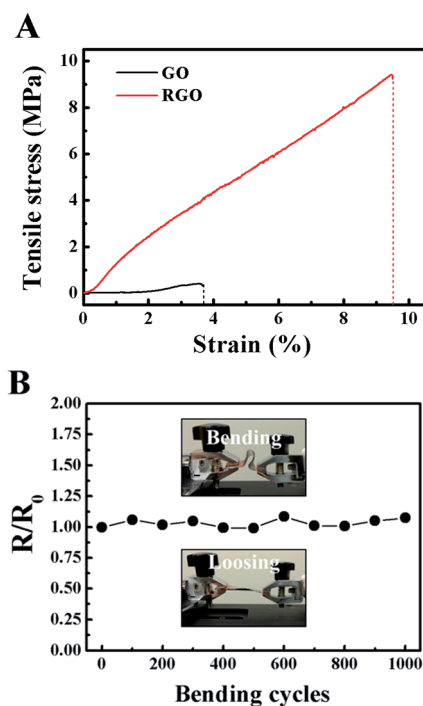


Fig. 3 (A) Tensile measurements of the GO and RGO papers. (B) Electrical resistance of an RGO paper (about  $4 \text{ cm} \times 6 \text{ cm}$ ,  $24 \text{ cm}^2$ ) with bending test:  $R_0$  and  $R$  correspond to the original resistance and resistance after bending. Inset shows the bending (above) and loosening (under) film.

### 3.3 Universal robust substrate for a high-performance SC electrode

To further investigate the robust RGO paper as a universal substrate for different active materials synthesized *via* different processing methods, two different kinds of electrodes with well-designed structures were fabricated by a hydrothermal ( $\text{WO}_3$ ) method and an electrodeposition (PPy) method, respectively, which are two representative processing methods for high-performance SCs<sup>4,36</sup> (Fig. 4A). One large free-standing flexible RGO paper is firstly cut into the appropriate size (*e.g.*  $5 \text{ cm} \times 2 \text{ cm}$ ,  $10 \text{ cm}^2$ ), and then polished with sandpaper along one direction; hence, the smooth surface of RGO paper becomes rougher and exhibits a unique fish scale-like structure, as shown in Fig. 4B. These micro fish scale-like RGO sheets, which are torn off from the bulk self-stacked RGO paper, ensure that more active materials could be loaded on to the substrate, which may result in a better electrochemical performance. Benefiting from the robust features, the polished RGO paper can bear both the hydrothermal and electrodeposition methods, turning the conductive substrate into a flexible electrode. As shown in Fig. 4C, after hydrothermal treatment,

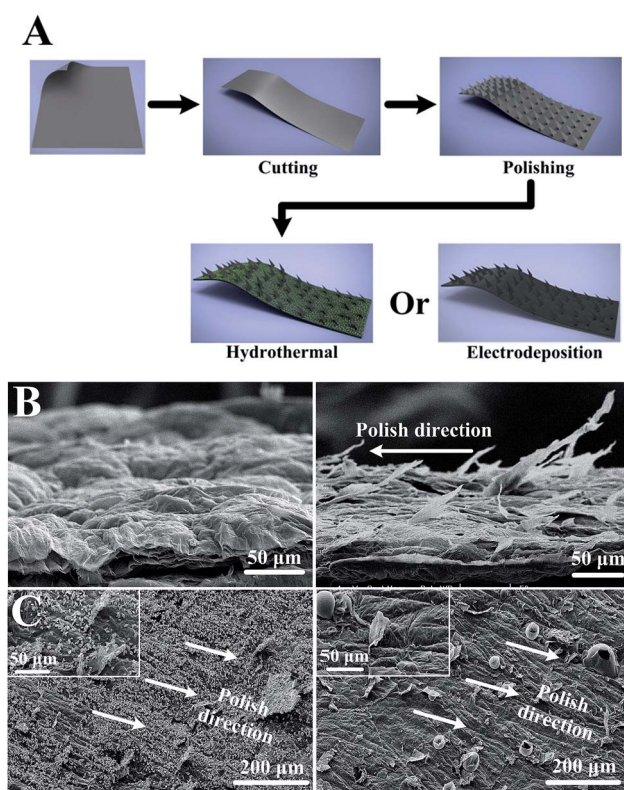
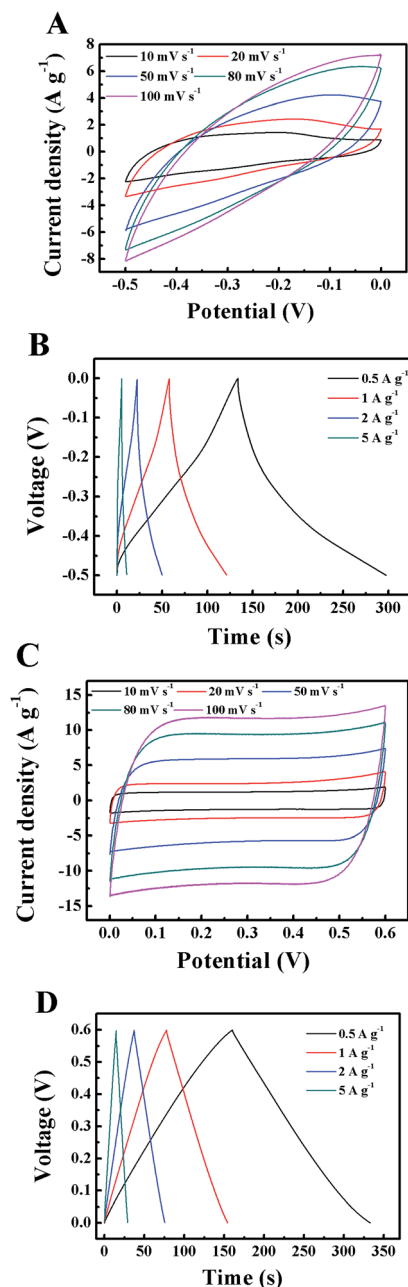
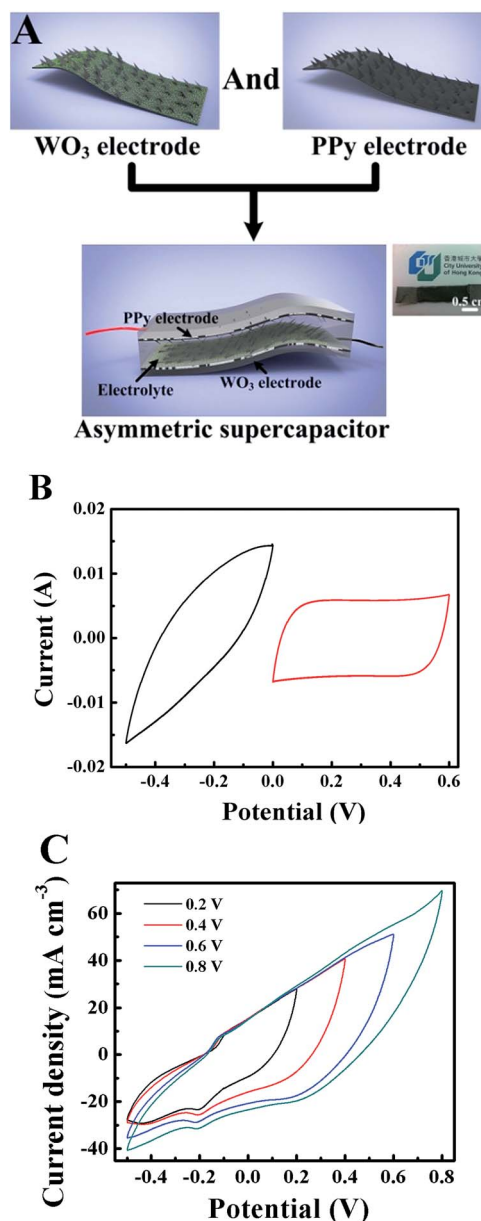


Fig. 4 (A) Schematic illustration of the fabrication process of  $\text{WO}_3$ - and PPy-RGO electrodes. One large free-standing flexible RGO substrate is firstly cut into appropriate size and then polished with sandpaper in one direction. Afterwards, the processed substrate is treated with a hydrothermal or electrodeposition method in order to load enough active materials on to its surface. (B) SEM images showing the RGO paper before polishing (left) and after polishing (right). (C) SEM images of  $\text{WO}_3$ -RGO (left) and PPy-RGO (right) paper electrodes. The insets are the high resolution images.



**Fig. 5** Electrochemical performance of the hydrothermal  $\text{WO}_3$ -RGO paper electrode in a three-electrode system: (A) CV at different scan rates of 10, 20, 50, 80, and  $100 \text{ mV s}^{-1}$  (from inner to outer). (B) Galvanostatic charge-discharge curves at different current densities of 0.5, 1, 2, and  $5 \text{ A g}^{-1}$ . Electrochemical performance of the electrodeposited PPy-RGO paper electrode in a three-electrode system: (C) CV at different scan rates of 10, 20, 50, 80, and  $100 \text{ mV s}^{-1}$  (from inner to outer). (D) Galvanostatic charge-discharge curves at different current densities of 0.5, 1, 2, and  $5 \text{ A g}^{-1}$ .

numerous nanoparticles, which were characterized to be  $\text{WO}_3$  (JCPDS no. 75-2187, Fig. S2†), are anchored both on the rough surface and on the fish scale-like sheets; however, after electrodeposition, the scratches and steps were clearly alleviated, since a thin layer of PPy, which is a typical conductive polymer, was successfully coated on the rough surface.



**Fig. 6** (A) Schematic of the fabrication process of the  $\text{WO}_3$ -RGO//PPy-RGO ASC. The inset is photograph of the all-solid asymmetric device. (B) Comparative CV of the  $\text{WO}_3$ - and PPy-RGO paper electrodes in a three-electrode system at a scan rate of  $100 \text{ mV s}^{-1}$ . (C) CVs of the  $\text{WO}_3$ -RGO//PPy-RGO ASC at different potential windows at a scan rate of  $100 \text{ mV s}^{-1}$ .

Due to their excellent conductivity and integrated structure, the free-standing  $\text{WO}_3$ -loaded and PPy-coated RGO papers can be directly used as SC electrodes. A three-electrode test configuration was employed to evaluate the electrochemical performance of both  $\text{WO}_3$ - and PPy-RGO paper electrodes. Fig. 5A and C show the CV loops of both electrodes in the range of  $10$ – $100 \text{ mV s}^{-1}$ . The CV curve of the  $\text{WO}_3$ -RGO electrode deviates from a rectangular shape, which can be attributed to the relatively large resistance, while the CV curve of PPy-RGO electrode is rectangular at the applied scan rates, indicating an

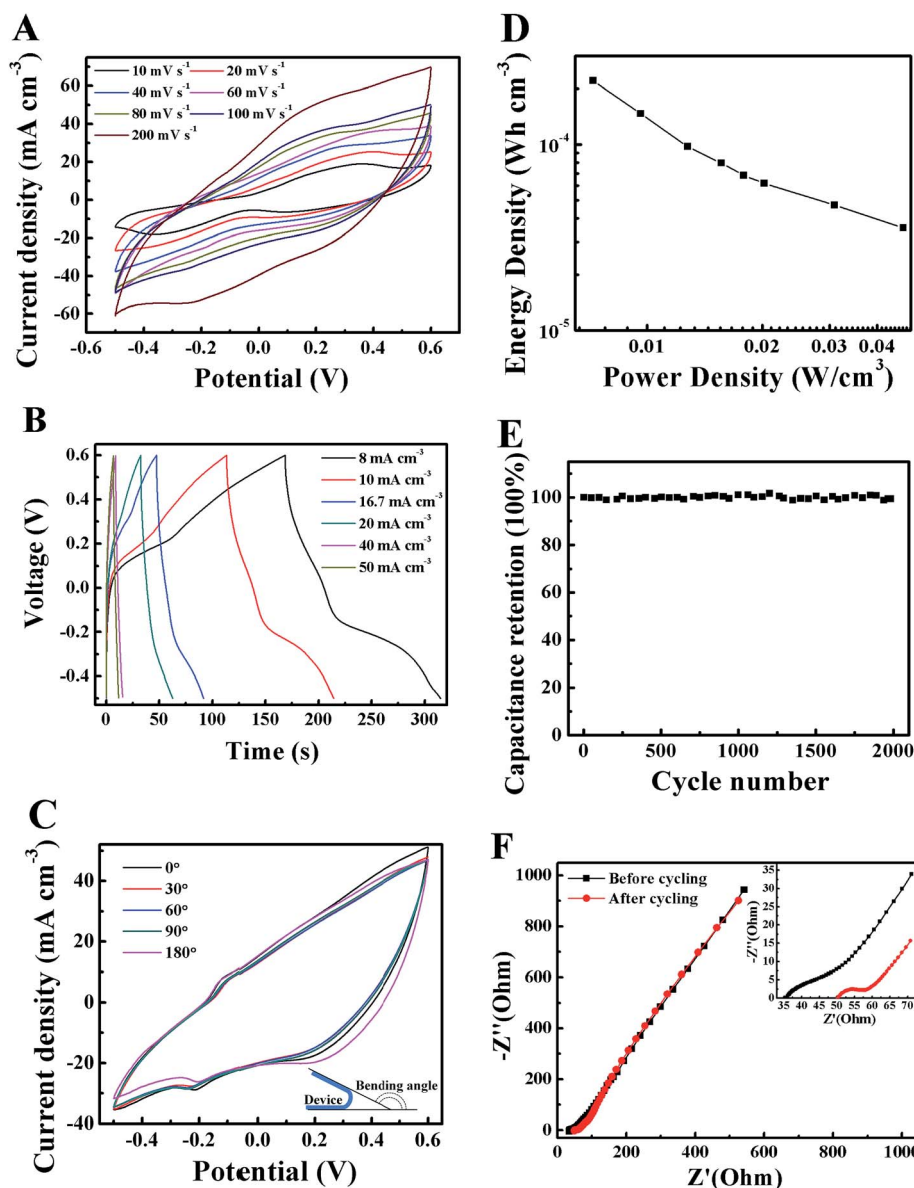


Fig. 7 Electrochemical performance of the  $\text{WO}_3\text{-RGO/PPy-RGO ASC}$ : (A) CVs at different scan rates of 10, 20, 40, 60, 80, 100, and 200  $\text{mV s}^{-1}$  (from inner to outer). (B) Galvanostatic charge-discharge curves at different current densities of 8, 10, 16.7, 20, 40, and 50  $\text{mA cm}^{-2}$ . (C) CVs of  $\text{WO}_3\text{-RGO/PPy-RGO ASC}$  at a scan rate of 100  $\text{mV s}^{-1}$  with different bending angles (an inward  $\sim 180^\circ$  bending angle). (D) Ragone plots of  $\text{WO}_3\text{-RGO/PPy-RGO ASC}$  based on the whole volume. (E) Capacitance retention ratio as a function of cycle numbers at an applied current of 8.3  $\text{mA cm}^{-2}$ . (F) Nyquist plots in the frequency range of 0.05 Hz to 100 kHz before and after 2000 cycles. The inset shows an enlarged EIS.

excellent capacitive behaviour and a low resistance.<sup>37</sup> The charge and discharge curves at different charge currents are shown in Fig. 5B and D. The deviation of the charge-discharge curves from the linear voltage-time relation of the  $\text{WO}_3\text{-RGO}$  electrode indicates a pseudo-capacitive behaviour (caused by the redox reactions),<sup>38</sup> whereas the curves of the PPy-RGO electrode are highly linear and symmetrical, suggesting a very good capacitive behaviour.<sup>39</sup> Moreover, no obvious  $iR$  drop is observed for any of the curves, indicating a rapid  $I$ - $V$  response and an excellent electrochemical reversibility.<sup>6</sup> The specific capacitance is calculated to be 123.4  $\text{F g}^{-1}$  ( $\text{WO}_3\text{-RGO}$ ) and 127.5  $\text{F g}^{-1}$  (PPy-RGO) at a current density of 1  $\text{A g}^{-1}$ , corresponding to area capacitance of 71  $\text{mF cm}^{-2}$  and 80  $\text{mF cm}^{-2}$ .

### 3.4 Assembly of a flexible all-solid state ASC

The robust freestanding RGO paper, which is compatible with distinctive active materials and can perfectly bear various processing methods, is an ideal substrate for flexible SC electrodes. To further demonstrate its promising application in high performance power devices with excellent flexibility, an all-solid state ASC was further fabricated by assembling the as-prepared  $\text{WO}_3\text{-}$  and PPy-RGO papers as negative and positive electrodes, respectively. The mass ratio of the two electrodes was fixed to 1.24, in order to achieve a charge balance between the negative and positive electrodes (Fig. 6A).



The stable operating potential windows for the  $\text{WO}_3$ - and PPY-RGO electrodes are  $-0.5$  to  $0$  V and  $0$  to  $0.6$  V, respectively (Fig. 6B). The cell voltage can be expressed as the sum of the potential range of the electrodes, and consequently the asymmetric device is expected to work within a voltage window of  $-0.5$  to  $0.6$  V. A series of CV measurements under different voltage windows are shown in Fig. 6C. The device exhibits a stable potential window even up to  $1.3$  V, which exceeds the theoretical decomposition voltage of water ( $1.23$  V) and could be ascribed to the high overpotential of hydrogen evolution on the electrode.<sup>40</sup>

CV curves at different scan rates (ranging from  $10$  to  $200$   $\text{mV s}^{-1}$ ) are collected in order to evaluate the performances of the  $\text{WO}_3$ -RGO//PPY-RGO ASC, as shown in Fig. 7A. The assembled full cells exhibit quasi-rectangular CV curves at low scan rates, which is attributed to the combination of the non-rectangular curves of  $\text{WO}_3$  and the rectangular curves of PPY, which agrees with a good capacitive behaviour.<sup>41</sup> Moreover, the CV curve still remains symmetrical even at a high scan rate of  $400$   $\text{mV s}^{-1}$  (Fig. S3†), indicating good reversibility of the electrochemical processes.<sup>40</sup> The charge-discharge curves show a symmetric charge and discharge process, and the deviation from the linear curve is attributed to the pseudo-capacitive behaviour of  $\text{WO}_3$ -RGO. The volumetric stack capacitance of the ASC was calculated to be  $1.31$   $\text{F cm}^{-3}$  at a scan rate of  $10$   $\text{mV s}^{-1}$ , which is much larger than the values reported for graphene ( $0.42$   $\text{F cm}^{-3}$ ),<sup>42</sup> TiN ( $0.33$   $\text{F cm}^{-3}$ )<sup>43</sup> SC and  $\text{H-TiO}_2\text{@MnO}_2/\text{H-TiO}_2\text{@C}$  ( $0.7$   $\text{F cm}^{-3}$ )<sup>44</sup> all-solid ASC. Correspondingly, the area capacitance was  $65.7$   $\text{mF cm}^{-2}$ , which was higher than the graphene-cellulose-paper-based SC ( $47$   $\text{mF cm}^{-2}$ ).<sup>20</sup> Note that compared with many other reported graphene-based planar films or papers,<sup>6,20,42</sup> our RGO paper is merely acting as a highly conductive flexible substrate and its contribution to the capacitance is very limited (Fig. S4†), which can eliminate the unnecessary distractions of capacitive performance and provide an accurate evaluation of the loaded active materials.

As per previous demonstrations, the RGO substrate exhibits outstanding flexibility and toughness. Thus, it is predictable that the ASC based on the RGO electrodes has great potential as a flexible power source. As shown in Fig. 7C, the perfectly overlapped CV curves at different bending angles indicate that the ASC can be bent to a large extent without degrading the performance. Moreover, even after being folded and unfolded to  $180^\circ$  over  $200$  times, the CV curves do not show an obvious change (Fig. S5†). A Ragone plot, which shows the energy and power densities (normalized to the whole device volume), is given in Fig. 7D. Significantly, our ASC possesses a high volumetric energy density of  $0.23$   $\text{mW h cm}^{-3}$  at a power density of  $7.3$   $\text{mW cm}^{-3}$ , which is comparable with or better than those of the previously reported flexible ASC or SCs such as hydrogenated  $\text{TiO}_2\text{@MnO}_2/\text{TiO}_2\text{@C}$ -based ASC ( $0.30$   $\text{mW h cm}^{-3}$ ),<sup>44</sup>  $\text{MnO}_2$ /carbon particles-based SC ( $0.09$   $\text{mW h cm}^{-3}$ ),<sup>45</sup> and graphene-based SC ( $0.06$   $\text{mW h cm}^{-3}$ ).<sup>42</sup> Moreover, our device shows remarkable cycling stability with a high capacitance retention of  $99.4\%$  over  $2000$  cycles at  $8.3$   $\text{mA cm}^{-3}$ , which is significant for practical applications. This outstanding cycling

performance is highly competitive with those of other reported ASCs such as  $\text{Co(OH)}_2$ /activated carbon ( $93\%$  retention after  $1000$  cycles),<sup>38</sup> graphene/ $\text{MnO}_2$ /activated carbon nanofiber ( $97\%$  retention after  $1000$  cycles),<sup>6</sup>  $\text{MnO}_2$ /activated carbon ( $96\%$  retention after  $1000$  cycles),<sup>46</sup> and  $\text{MnO}_2$ /functional mesoporous carbon nanotubes ( $90\%$  retention after  $1000$  cycles).<sup>47</sup> EIS was used to investigate the resistance change of the ASC before and after the cycling test. After  $2000$  cycles, nearly no change was observed for  $R_{\text{ct}}$  ( $\Omega$ ), and only a slight increase of  $R_s$  from  $36$  to  $50$   $\Omega$  was observed. These EIS results further demonstrate the exceptional stability of our flexible ASC, which is attributed to the robust RGO substrate.

## 4. Conclusions

In summary, inspired by cooking an omelette, a large area freestanding pristine GO paper was firstly fried using a non-stick frying pan. This was followed by post-reductions, when the GO paper was reduced to RGO paper with excellent electrical and mechanical properties, as well as outstanding flexibility and robustness. In particular, this ingenious method can fabricate RGO papers in a variety of sizes and thicknesses just by simply changing the frying pan or the concentration of the GO solution. The as-fabricated RGO papers are very robust, being able to bear sandpaper polishing, bending, folding, and hydrothermal and electrochemical deposition processes without any structure/performance degradation. As a demonstration, two flexible RGO-based electrodes were fabricated *via* hydrothermal and electrodeposition methods with  $\text{WO}_3$  and PPY as the active materials, respectively. The as-obtained  $\text{WO}_3$ - and PPY-RGO electrodes were further assembled into an all-solid ASC, which achieved a high energy density of  $0.23$   $\text{mW h cm}^{-3}$  at a power density of  $7.3$   $\text{mW cm}^{-3}$  and an outstanding retention rate of  $99.4\%$  after  $2000$  cycles. In addition, benefiting from the robust features of RGO paper, the flexible all-solid ASC possesses a great deformation tolerance. Consequently, the robust RGO paper, as developed by our facile, low-cost and scalable method, can be applied to fabricate high performance flexible power sources, thus showing great potential for portable wearable electronic devices.

## Acknowledgements

This research was supported by the Early Career Scheme of the Research Grants Council of Hong Kong SAR, China (under Project Numbers City U 9041977), the Science Technology and Innovation Committee of Shenzhen Municipality (Grant number R-IND4901), and a grant from the City University of Hong Kong.

## Notes and references

- 1 Z. Liu, J. Xu, D. Chen and G. Shen, *Chem. Soc. Rev.*, 2015, **44**, 161–192.
- 2 G. Shen, L. Liao, C. Zhou and Y. Bando, *J. Mater. Chem. C*, 2014, **2**, 1176–1177.
- 3 Z. Zhang, J. Deng, X. Li, Z. Yang, S. He, X. Chen, G. Guan, J. Ren and H. Peng, *Adv. Mater.*, 2015, **27**, 356–362.



- 4 Y. Huang, J. Tao, W. Meng, M. Zhu, Y. Huang, Y. Fu, Y. Gao and C. Zhi, *Nano Energy*, 2015, **11**, 518–525.
- 5 W. Tian, X. Wang, C. Zhi, T. Zhai, D. Liu, C. Zhang, D. Golberg and Y. Bando, *Nano Energy*, 2013, **2**, 754–763.
- 6 Z. Fan, J. Yan, T. Wei, L. Zhi, G. Ning, T. Li and F. Wei, *Adv. Funct. Mater.*, 2011, **21**, 2366–2375.
- 7 J. Tao, N. Liu, L. Li, J. Su and Y. Gao, *Nanoscale*, 2014, **6**, 2922–2928.
- 8 S. Wang, N. Liu, J. Tao, C. Yang, W. Liu, Y. Shi, Y. Wang, J. Su, L. Li and Y. Gao, *J. Mater. Chem. A*, 2015, **3**, 2407–2413.
- 9 R. Ma, X. Liu, J. Liang, Y. Bando and T. Sasaki, *Adv. Mater.*, 2014, **26**, 4173–4178.
- 10 X. Lu, T. Zhai, X. Zhang, Y. Shen, L. Yuan, B. Hu, L. Gong, J. Chen, Y. Gao, J. Zhou, Y. Tong and Z. L. Wang, *Adv. Mater.*, 2012, **24**, 938–944.
- 11 P. Li, Y. Yang, E. Shi, Q. Shen, Y. Shang, S. Wu, J. Wei, K. Wang, H. Zhu, Q. Yuan, A. Cao and D. Wu, *ACS Appl. Mater. Interfaces*, 2014, **6**, 5228–5234.
- 12 B. Yao, L. Yuan, X. Xiao, J. Zhang, Y. Qi, J. Zhou, J. Zhou, B. Hu and W. Chen, *Nano Energy*, 2013, **2**, 1071–1078.
- 13 L. Yuan, X. Xiao, T. Ding, J. Zhong, X. Zhang, Y. Shen, B. Hu, Y. Huang, J. Zhou and Z. L. Wang, *Angew. Chem., Int. Ed.*, 2012, **124**, 5018–5022.
- 14 A. K. Geim and K. S. Novoselov, *Nat. Mater.*, 2007, **6**, 183–191.
- 15 A. K. Geim, *Science*, 2009, **324**, 1530–1534.
- 16 K. S. Kim, Y. Zhao, H. Jang, S. Y. Lee, J. M. Kim, K. S. Kim, J.-H. Ahn, P. Kim, J.-Y. Choi and B. H. Hong, *Nature*, 2009, **457**, 706–710.
- 17 A. L. M. Reddy, A. Srivastava, S. R. Gowda, H. Gullapalli, M. Dubey and P. M. Ajayan, *ACS Nano*, 2010, **4**, 6337–6342.
- 18 M. J. Allen, V. C. Tung and R. B. Kaner, *Chem. Rev.*, 2009, **110**, 132–145.
- 19 X. Wang, Y. Zhang, C. Zhi, X. Wang, D. Tang, Y. Xu, Q. Weng, X. Jiang, M. Mitome, D. Golberg and Y. Bando, *Nat. Commun.*, 2013, **4**, 1–8.
- 20 Z. Weng, Y. Su, D.-W. Wang, F. Li, J. Du and H.-M. Cheng, *Adv. Energy Mater.*, 2011, **1**, 917–922.
- 21 S. Pei, J. Zhao, J. Du, W. Ren and H.-M. Cheng, *Carbon*, 2010, **48**, 4466–4474.
- 22 M. Wang, L. D. Duong, J.-S. Oh, N. T. Mai, S. Kim, S. Hong, T. Hwang, Y. Lee and J.-D. Nam, *ACS Appl. Mater. Interfaces*, 2014, **6**, 1747–1753.
- 23 K. Rana, S. D. Kim and J.-H. Ahn, *Nanoscale*, 2015, DOI: 10.1039/c4nr06082b.
- 24 W. S. Hummers and R. E. Offeman, *J. Am. Chem. Soc.*, 1958, **80**, 1339.
- 25 M. Zhu, W. Meng, Y. Huang, Y. Huang and C. Zhi, *ACS Appl. Mater. Interfaces*, 2014, **6**, 18901–18910.
- 26 B. Shen, W. Zhai and W. Zheng, *Adv. Funct. Mater.*, 2014, **24**, 4542–4548.
- 27 G. Xin, H. Sun, T. Hu, H. R. Fard, X. Sun, N. Koratkar, T. Borca-Tasciuc and J. Lian, *Adv. Mater.*, 2014, **26**, 4521–4526.
- 28 C. Chen, Q.-H. Yang, Y. Yang, W. Lv, Y. Wen, P.-X. Hou, M. Wang and H.-M. Cheng, *Adv. Mater.*, 2009, **21**, 3007–3011.
- 29 D.-W. Wang, F. Li, J. Zhao, W. Ren, Z.-G. Chen, J. Tan, Z.-S. Wu, I. Gentle, G. Q. Lu and H.-M. Cheng, *ACS Nano*, 2009, **3**, 1745–1752.
- 30 G. Eda, G. Fanchini and M. Chhowalla, *Nat. Nanotechnol.*, 2008, **3**, 270–274.
- 31 J. Che, L. Shen and Y. Xiao, *J. Mater. Chem.*, 2010, **20**, 1722–1727.
- 32 C. Mattevi, G. Eda, S. Agnoli, S. Miller, K. A. Mkhoyan, O. Celik, D. Mastrogianni, G. Granozzi, E. Garfunkel and M. Chhowalla, *Adv. Funct. Mater.*, 2009, **19**, 2577–2583.
- 33 A. Gupta, G. Chen, P. Joshi, S. Tadigadapa and P. C. Eklund, *Nano Lett.*, 2006, **6**, 2667–2673.
- 34 A. C. Ferrari, J. C. Meyer, V. Scardaci, C. Casiraghi, M. Lazzeri, F. Mauri, S. Piscanec, D. Jiang, K. S. Novoselov, S. Roth and A. K. Geim, *Phys. Rev. Lett.*, 2006, **97**, 187401.
- 35 D. P. Dubal, J. G. Kim, Y. Kim, R. Holze, C. D. Lokhande and W. B. Kim, *Energy Technol.*, 2014, **2**, 325–341.
- 36 W. Meng, W. Chen, L. Zhao, Y. Huang, M. Zhu, Y. Huang, Y. Fu, F. Geng, J. Yu, X. Chen and C. Zhi, *Nano Energy*, 2014, **8**, 133–140.
- 37 L. Hu, W. Chen, X. Xie, N. Liu, Y. Yang, H. Wu, Y. Yao, M. Pasta, H. N. Alshareef and Y. Cui, *ACS Nano*, 2011, **5**, 8904–8913.
- 38 L.-B. Kong, M. Liu, J.-W. Lang, Y.-C. Luo and L. Kang, *J. Electrochem. Soc.*, 2009, **156**, A1000–A1004.
- 39 R. Liu and S. B. Lee, *J. Am. Chem. Soc.*, 2008, **130**, 2942–2943.
- 40 J. Liu, L. Zhang, H. B. Wu, J. Lin, Z. Shen and X. W. Lou, *Energy Environ. Sci.*, 2014, **7**, 3709–3719.
- 41 T. Cottineau, M. Toupin, T. Delahaye, T. Brousse and D. Bélanger, *Appl. Phys. A*, 2006, **82**, 599–606.
- 42 M. F. El-Kady, V. Strong, S. Dubin and R. B. Kaner, *Science*, 2012, **335**, 1326–1330.
- 43 X. Lu, G. Wang, T. Zhai, M. Yu, S. Xie, Y. Ling, C. Liang, Y. Tong and Y. Li, *Nano Lett.*, 2012, **12**, 5376–5381.
- 44 X. Lu, M. Yu, G. Wang, T. Zhai, S. Xie, Y. Ling, Y. Tong and Y. Li, *Adv. Mater.*, 2013, **25**, 267–272.
- 45 L. Yuan, X.-H. Lu, X. Xiao, T. Zhai, J. Dai, F. Zhang, B. Hu, X. Wang, L. Gong, J. Chen, C. Hu, Y. Tong, J. Zhou and Z. L. Wang, *ACS Nano*, 2011, **6**, 656–661.
- 46 H.-Q. Wang, Z.-S. Li, Y.-G. Huang, Q.-Y. Li and X.-Y. Wang, *J. Mater. Chem.*, 2010, **20**, 3883–3889.
- 47 H. Jiang, C. Li, T. Sun and J. Ma, *Nanoscale*, 2012, **4**, 807–812.